Turbulence and Energy Dissipation from Wave Breaking

JIARONG WU,[a,b] STÉPHANE POPINET,[c] BERTRAND CHAPRON,[d] J. THOMAS FARRAR,[e] AND LUC DEIKE[a]

[a] *Princeton University, Princeton, New Jersey*
[b] *Courant Institute of Mathematical Sciences, New York University, New York, New York*
[c] *Sorbonne Université, CNRS, Institut Jean Le Rond d'Alembert, Paris, France*
[d] *Ifremer, LOPS, Brest, France*
[e] *Woods Hole Oceanographic Institution, Woods Hole, Massachusetts*

(Manuscript received 6 March 2025, in final form 12 May 2025, accepted 2 June 2025)

ABSTRACT: Wave breaking is a critical process in the upper ocean: an energy sink for the surface wave field and a source for turbulence in the ocean surface boundary layer. We apply a novel multilayer numerical solver resolving upper-ocean dynamics over scales from $O(50)$ cm to $O(1)$ km, including a broadbanded wave field and wave breaking. The present numerical study isolates the effect of wave breaking and allows us to study the surface layer in wave-influenced and wave-breaking-dominated regimes. Following our previous work showing wave-breaking statistics in agreement with field observations, we extend the analysis to underwater breaking-induced turbulence and related dissipation (in freely decaying conditions). We observe a rich field of vorticity resulting from the turbulence generation by breaking waves. We discuss the vertical profiles of dissipation rate, which are compared with field observations, and propose an empirical universal shape function. Good agreement is found, further demonstrating that wave breaking can dominate turbulence generation in the near-surface layer. We examine the dissipation from different angles: the global dissipation of the wave field computed from the decaying wave field, the spectral dissipation from the fifth moment of the breaking front distribution, and a turbulence dissipation estimated from the underwater strain-rate tensor. Finally, we consider how these different estimates can be understood as part of a coherent framework.

KEYWORDS: Wave breaking; Wind waves; Atmosphere-ocean interaction; Oceanic mixed layer; Surface layer; Numerical analysis/modeling

1. Introduction

The top few meters of the oceanic boundary layer are heavily affected by the wind and surface waves. Wind is the major driving force for the large-scale ocean circulation (Ferrari and Wunsch 2009). To a large extent, the wind stress acts on the upper ocean indirectly, by first amplifying the wave field, especially under high winds (Wang and Huang 2004). Then, the locally saturated wave field undergoes wave breaking, which deposits momentum and energy into the current and upper-ocean turbulence (Sullivan and McWilliams 2010). Wave breaking thus acts as a sink for the wave energy but as a source for upper-ocean currents and turbulent kinetic energy (TKE). However, the energy pathway from the wind into the surface waves and eventually into the upper ocean current (mean flow) and turbulence (fluctuation) is not well characterized, largely due to the difficulty of making measurements in the vicinity of the sometimes violently moving air–sea interface.

This paper is devoted to understanding the process of turbulence generation and dissipation associated with broadbanded surface wave breaking in the ocean surface layer, i.e., the uppermost few meters of the ocean boundary layer (OBL). While nonbreaking waves can interact with the upper ocean through mechanisms such as Stokes drift and Langmuir circulation (Sullivan and McWilliams 2010), this study focuses specifically on turbulence induced by breaking waves. In surface OBL studies, the vertical profile of the turbulent energy dissipation rate has been widely used as a key characteristic of turbulence under varying wind and wave conditions. This is largely because the dissipation rate is more readily measurable in the field compared to other turbulent statistics, such as the turbulent fluxes. Thus, it serves as a more reliable metric for comparing observational data with predictions from turbulence closure models.

Field observations of dissipation rate profiles in the surface OBL have been conducted despite the technical challenges of near-surface measurements (Anis and Moum 1995; Drennan et al. 1996; Terray et al. 1996; Soloviev and Lukas 2003; Gerbi et al. 2009; Sutherland and Melville 2015a; Thomson et al. 2016; Zippel et al. 2018; Miller et al. 2023, etc.). Turbulence is typically measured using fixed sensors or rising profilers, with dissipation rates derived from turbulence spectra or structure functions. These studies show that wave breaking can enhance dissipation by up to an order of magnitude compared to law-of-the-wall predictions. Most also report deviations from the classic z^{-1} scaling in an intermediate depth range (Terray et al. 1996; Sutherland and Melville 2015a), though some contradictory evidence exists (Esters et al. 2018). Observations of breaking-induced currents are sparse (notably Kudryavtsev et al. 2008), likely due to difficulties in isolating them from wave orbital motions and the general challenge of current measurements near the surface.

In terms of modeling efforts, the effects of wave breaking on upper-ocean turbulence and current are limited to low-order representations and are not routinely included in OBL models.

Corresponding author: Luc Deike, ldeike@princeton.edu

DOI: 10.1175/JPO-D-25-0052.1

Existing Reynolds-averaged Navier–Stokes (RANS) frameworks typically model breaking as a source term in the TKE equation and/or momentum equation, with the goal of reproducing observed dissipation profiles (Rascle et al. 2013). The input can be either at the surface for TKE (Craig and Banner 1994) or with a prescribed injection depth (Kudryavtsev et al. 2008; Sullivan et al. 2007) for both TKE and momentum. The other modeling choice involves how to represent the spectral distribution of breaking waves: either waves of all scales are considered together using bulk parameters, or certain empirical breaking distributions are prescribed. Other modeling approaches include using an empirically determined dissipation profile (together with assumptions about mixing length) to directly model-breaking-induced mixing (Romero et al. 2021).

More sophisticated large-eddy simulation (LES) modeling (e.g., Sullivan et al. 2007) is of higher resolution and fidelity than RANS models, but it is not routinely used in practice due to the higher computational cost. In Sullivan et al. (2007), breakers are randomly sampled from an empirical breaking probability distribution with certain global constraints of momentum and energy conservation, and each breaker is modeled by a self-similar momentum and energy entrainment profile. In addition, wave–current interaction is modeled by including a vortex force. This work suggests that overall OBLs behave differently from purely shear-driven turbulent boundary layers due to the existence of surface waves, and the effects of realistic intermittent wave breaking depend on the breaking distribution.

The current study aims to numerically investigate the breaking distribution and the associated underwater turbulent field as an emergent phenomenon of broadband wave spectra. In our previous paper (Wu et al. 2023, hereafter W23), we introduced the use of the novel multilayer numerical method (Popinet 2020) for modeling breaking-wave fields. The simulations have similar scale and resolution to the work of Sullivan et al. (2007), but a fundamentally different treatment of wave breaking. In our framework, the breaking events are not sampled from a prescribed distribution but emerge naturally through focusing and are detected using a geometric criterion of the free surface. No subgrid entrainment models are needed since we are directly approximating the Navier–Stokes equations and are resolving the breaking events and their effects. In W23, we characterized the breaking kinematics and statistics based on free-surface elevation following the framework first introduced by Phillips (1985) and found good agreement with field observations (Schwendeman et al. 2014; Sutherland and Melville 2013; Kleiss and Melville 2010, etc.). Based on the numerical results, we proposed a new scaling for the distribution of breaking crest length using wave-spectrum-related quantities (peak phase speed and mean square slope). By showing the predictive power of the proposed scaling on existing observational data, we further confirmed the direct link between the surface wave spectrum and breaking distribution.

In this paper, we investigate the upper-ocean turbulent fields associated with broadbanded wave breaking. We first show vorticity generation by breaking (concentrated in the top few meters of wave-influenced layer). Then, we focus on an analysis of the vertical structure of the dissipation rate (estimated from the strain-rate tensor) and the total dissipation of the system. The effect of wave breaking is isolated due to the fact that we are analyzing short time-scale behaviors [$O(10)$ peak wave periods] without a development of wave–current interaction and that, by construction, there is no wind forcing. Results are compared with field observations of dissipation rate profiles and discussed in the context of OBL modeling.

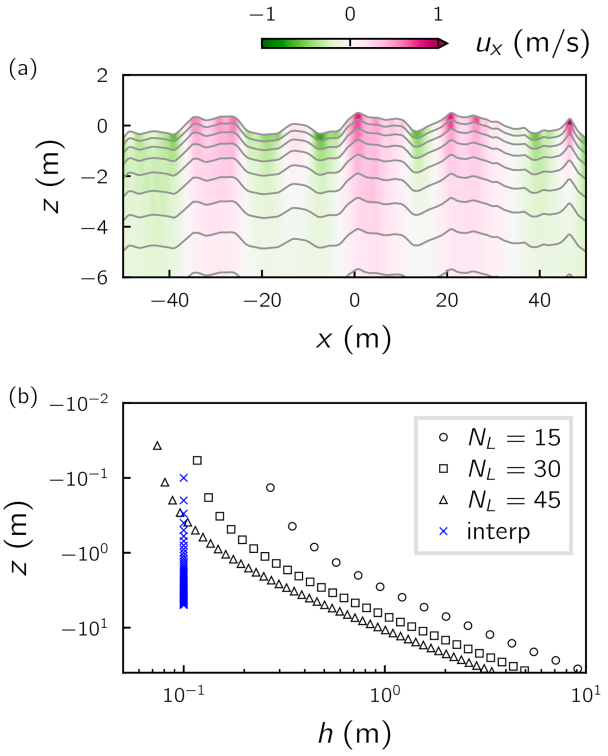

FIG. 1. (a) Illustration of the layered discretization for $N_L = 15$ (for only part of the domain). Color shows the horizontal velocity, and the gray lines show the layers. (b) The geometric distribution of layer thickness. The blue marks are the uniformly spaced interpolation points used in the analysis in Fig. 7.

2. Numerical methods

a. Governing equation and numerical solver

The numerical setup follows W23 and uses the multilayer numerical solver (Popinet 2020; Wu 2023). An example of the multilayer discretization with the free surface is shown in Fig. 1a. We solve the Navier–Stokes equations written as a set of layered equations (Popinet 2020), with the most general form of the governing equations being given by

$$\partial_t h_l + \nabla_H \cdot (h\mathbf{u})_l = 0, \tag{1}$$

$$\partial_t (h\mathbf{u})_l + \nabla_H \cdot (h\mathbf{u}\mathbf{u})_l = -g h_l \nabla_H \eta - \nabla_H (h\phi)_l + [\phi \nabla_H z]_l + [\nu_1 \partial_z \mathbf{u}]_l + \nu_2 \nabla_H^2 \mathbf{u}, \tag{2}$$

$$\partial_t (hw)_l + \nabla_H \cdot (hw\mathbf{u})_l = -[\phi]_l + [\nu_1 \partial_z w]_l + \nu_2 \nabla_H^2 w, \tag{3}$$

$$\nabla_H \cdot (h\mathbf{u})_l + [w - u \cdot \nabla_H z]_l = 0, \tag{4}$$

with l being the index of the layer, h being its thickness, z being its vertical position, $\mathbf{u} = (u, v)$, w is the horizontal and vertical components of the velocity, ϕ is the nonhydrostatic pressure (divided by density), $g = 9.8\ \mathrm{m\ s^{-1}}$ is the gravitational acceleration, and ν_1 and ν_2 are the vertical and horizontal (kinematic) viscosity coefficients. Values of the kinematic viscosity are chosen small enough to ensure limited dissipation by nonbreaking waves, and dissipation due to breaking will be associated with an effective numerical viscosity. The surface elevation $\eta = z_b + \sum_{l=0}^{N_L} h_l$, and the $[]_l$ operator denotes the vertical difference, i.e., $[f]_l = f_{l+1/2} - f_{l-1/2}$. Equation (1) means that the layer thicknesses h_l follow material surfaces (i.e., the discretization is vertically Lagrangian). Equations (2) and (3) are the horizontal and vertical momentum equations. Equation (4) is the mass conservation equation (used to implement the incompressibility conditions). The anisotropy of the grid makes it a reasonable option to use different horizontal and vertical viscosities. We specify a small value of physical viscosity, while the dissipative effects in the numerical system are dominated by numerical viscosity and the gradient limiter [Eq. (5)].

In terms of numerical resolution, the domain size is $(L_x, L_y, L_z) = (200, 200, 40)$ m with (N_H, N_H, N_L) grid points. The horizontal grid is evenly spaced, and we use $N_H = 1024$ (for a numerical convergence test on horizontal resolution, see W23). The vertical grid spacing follows a geometric series, and the averaged layer depths for $N_L = 15, 30, 45$ are shown in Fig. 1b; the thickness of the topmost layer is 0.27, 0.12, and 0.07 m, respectively. The vertical layers are more concentrated toward the surface with a thickness ratio of 1.2 between adjacent layers. Aside from the breaking model described in the next section, there is no explicit subgrid-scale turbulence model: the effect of any unresolved subgrid-scale structure is assumed to be adequately approximated by numerical diffusion (see W23 for a discussion).

b. Modeling of wave breaking

The dissipative effect on waves due to wave breaking is modeled by a gradient limiter. The horizontal gradient $\partial z/\partial x$ for any layer in Eqs. (2) and (4) is limited by a maximum value $s_{\max}$:

$$\partial z/\partial x = \begin{cases} \partial z/\partial x, & |\partial z/\partial x| \le s_{\max} \\ \mathrm{sign}(\partial z/\partial x) s_{\max}, & |\partial z/\partial x| > s_{\max} \end{cases}. \tag{5}$$

Note that the wave slope (or the slope between any layer) itself is not affected by this limiter [only its gradient used in Eqs. (2) and (4)]. The solutions are not particularly sensitive to the value of $s_{\max}$ and a value of 0.577 is chosen (see W23 for validations). Overturning of the free surface cannot occur in the multilayer model, as the surface elevation η is a single-valued function. As a result, breaking dynamics are shock-like (Brocchini and Dodd 2008). Still, the multilayer solver includes additional dissipative and dispersive effects that are not present in the pure shallow-water model.

TABLE 1. A compilation of cases and their steepness parameters. The ranges of σ and H_s indicate the variability within the sampling window.

Label	$Pg^{-1/2}$ ($\mathrm{m^{1/2}}$)	k_p ($\mathrm{m^{-1}}$)	σ	H_s (m)
P008	0.008	0.157	[0.099, 0.103]	[0.983, 0.986]
P01	0.01		[0.116, 0.122]	[1.097, 1.104]
P016	0.016		[0.145, 0.147]	[1.341, 1.359]
P02	0.02		[0.150, 0.154]	[1.442, 1.460]
P03	0.03		[0.161, 0.165]	[1.697, 1.735]

c. Broadband wave field simulations

We initialize the wave field with a directional wavenumber spectrum $\phi(k, \theta)$ derived from an azimuth-integrated wavenumber spectrum $\phi(k)$ typical of wind waves:

$$\phi(k) = Pg^{-1/2}k^{-5/2}\exp[-1.25(k_p/k)^2]. \tag{6}$$

The spectrum is a combination of an f^{-4} asymptotic tail and a Pierson–Moskowitz shape function $\exp[-1.25(k_p/k)^2]$ (Elfouhaily et al. 1997). The f^{-4} tail is predicted for the equilibrium range (Phillips 1985) and observed in the field (Lenain and Melville 2017). The directional spreading is proportional to $\cos^N(\theta)$ with $N = 5$. The value of P (of dimension $\mathrm{m\ s^{-1}}$) controls how energetic the wave field is, while k_p is the peak wavenumber of the spectrum. We use $k_p = 2\pi/40 = 0.157\ \mathrm{m^{-1}}$ ($\omega_p = 1.24\ \mathrm{s^{-1}}$) for all the cases presented here. For this peak wavenumber, the computational domain is large enough both in the horizontal direction to avoid confinement effects and in the vertical direction to ensure that the wave dynamics do not depend on the bottom boundary.

The initial wave field is a superposition of linear waves $\eta = \sum_{i,j} a_{ij}\cos(\psi_{ij})$, with the amplitude $a_{ij} = [2\phi(k_{xi}, k_{yj})dk_x dk_y]^{1/2}$ and the initial random phase $\psi_{ij} = k_{xi}x + k_{yj}y + \psi_{\mathrm{rand}ij}$. The corresponding orbital velocity is initialized similarly according to the linear wave relation. Only a few long-wave components are used for initialization with cutoffs at $32k_p/5$ in the x direction and $16k_p/5$ in the y direction (see W23). After initialization, the wave field evolves, undergoes intermittent breaking due to random focusing, and develops the short-wave tail over time (largely through wave breaking). The evolution of the wave field and the spectral shape are discussed in detail in W23. Here, we focus on the latter stage when the spectral shape is quasi-stationary while the energy of the wave field slowly decays. We note that the results are not sensitive to the choice of the initial spectral shape as the k^{-3} tail naturally develops through wave breaking.

The value of P roughly corresponds to different wind speeds, assuming similarity in the shape of the spectra. It is chosen to range from 0.08 (almost no breaking) to 0.3 (steep, actively breaking) in the simulations, and it is used for labeling cases listed in Table 1. We also define two diagnostic variables: the root-mean-square slope (rmss),

$$\sigma = \left[\int_0^\infty k^2\phi(k)dk\right]^{1/2}, \tag{7}$$

and the significant wave height,

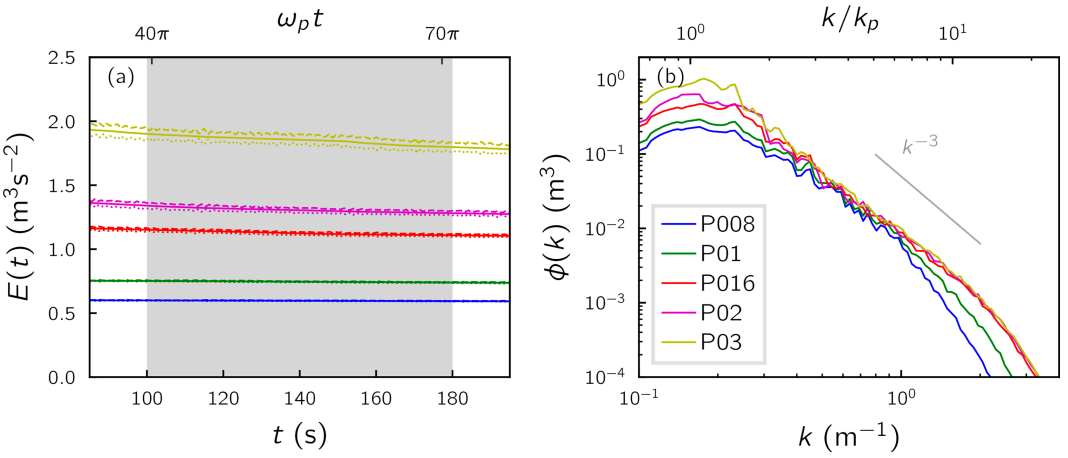

FIG. 2. (a) Energy evolution of each case showing that the system is slowly decaying without external forcing. Because equipartition of kinetic and potential energy is expected for linear waves, we show twice the kinetic energy, $2E_k$ (dashed lines); twice the potential energy, $2E_p$ (dotted lines); and the total energy, $E = E_k + E_p$ (solid lines). The sampling period is indicated with the gray shading. (b) The spectra of each case at the start of the sampling period $t = 100$ s. For both plots, the color of the lines indicates the different initial spectrum P value listed in Table 1. The bottom horizontal axis shows dimensional variables, while the top horizontal axis shows nondimensional variables normalized by peak wavenumber k_p or peak frequency ω_p.

$$H_s = 4\langle\eta^2\rangle^{1/2} = 4\left[\int_0^\infty \phi(k)dk\right]^{1/2}, \tag{8}$$

where the angle brackets denote horizontal averaging. In practice, the integrals are taken over numerically resolved wavenumbers. Table 1 summarizes the values of σ and H_s for different initial values of P. In general, the initial condition P, rmss σ, and significant wave height H_s are positively correlated, but σ and H_s characterize different aspects of the wave field. The H_s value indicates the energy content and is largely determined by the low-wavenumber spectral peak, while the σ value indicates the roughness of the (numerically resolved) surface and is heavily influenced by the high-wavenumber part of the spectrum. Their values for a given initial P are specific to the current setup.

Figure 2a shows the energy evolution for each case with the sampling window indicated in gray shade. Figure 2b shows the spectral shape at the start of the sampling window ($t = 100$). Here, the energy of the system E is defined as the sum of volume-integrated potential energy ($E_p = \iint g\eta^2 dxdy/2$, dashed lines) and kinetic energy ($E_k = \iiint |\mathbf{u}|^2 dxdydz$, dotted lines). The kinetic energy is slightly higher than the potential energy because of the existence of nonwave motion. The wave energy is $E_w = 2E_p = \iint g\eta^2 dxdy$ assuming equipartition of potential and kinetic energy for the waves. The energy of the wave field steadily decays without any external forcing due to breaking, and we see the fastest decay for the steepest case due to more frequent breaking. The small discrepancy between the total energy of the system E and the wave energy E_w does not affect the discussion of the decay rate, as we found $dE/dt \approx dE_w/dt$.

The total integration window in the quasi-stationary phase is relatively short (on the order of 15 peak wave periods). There are two main reasons for this choice: first, in this study, we focus on the short-term effects of breaking in generating current and turbulence; second, we are limited by the dissipative nature of the simulation (which is an intrinsic limitation of the current setup). Future implementations will add boundary wind–like forcing to balance the dissipation so that the long-term wave effects on the upper-ocean boundary layer can be studied. The range of (numerically resolved) rmss and significant wave height in the sampling window is listed in Table 1.

3. Diagnosis

Figure 3 shows a 3D visualization of the simulation that demonstrates the surface geometry of the broadband wave field and the rich vorticity field. In the following sections, we describe the diagnosis of both the breaking statistics at the surface and the current and turbulence in the interior.

a. Breaking front distribution

Despite there being no overturning in the simulation, the breaking fronts are characterized by the sharp ridge-like features of the surface. In the rest of the paper, we refer to this localized sharpening of the surface in the numerical simulation as "breaking." Such sharpening induces strong dissipation and generates vorticity similar to actual breaking events. We perform breaking front detection based on a Gaussian curvature criterion, and the procedure and sensitivity studies are discussed in detail in W23.

The main result of W23 is that the distribution $\Lambda(c)$, defined as the length of breaking front per unit area moving with speed in the vicinity of c (Phillips 1985), is self-similar for wave fields of similar spectral shape but different steepness σ and peak phase speed c_p. A scaling using only wave field features (i.e., peak wave phase speed c_p and rmss σ) was proposed and tested on field observations. Figure 4 shows the $\Lambda(c)$ distribution, as well as premultiplied by c^5, without rescaling. The fifth

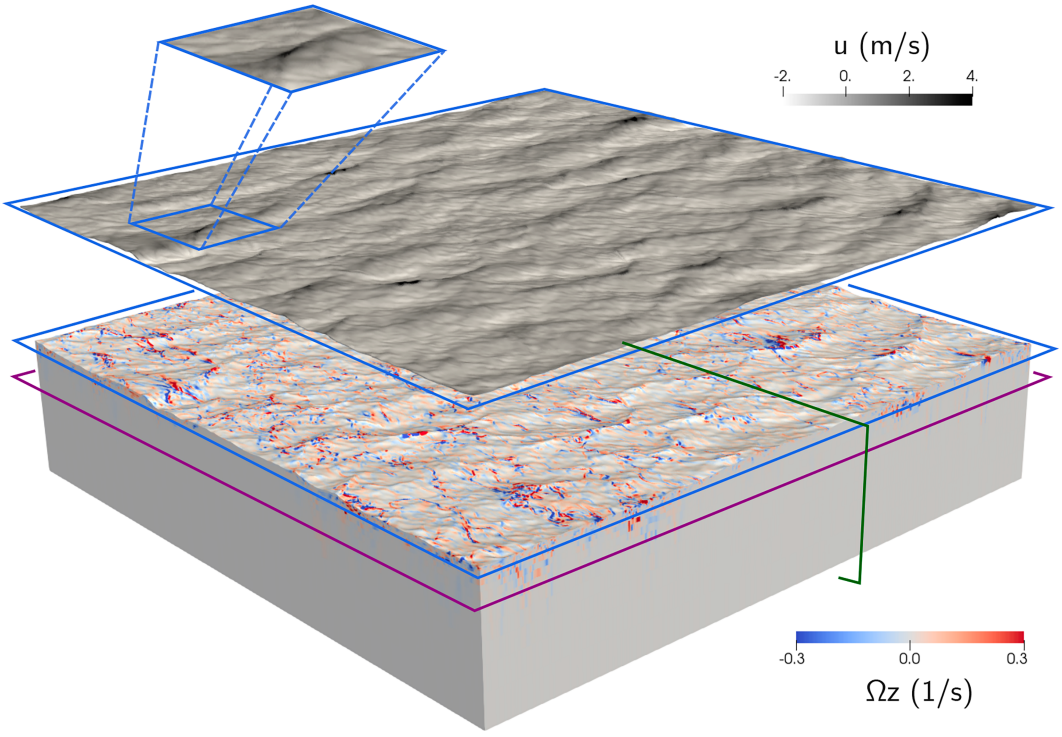

FIG. 3. 3D illustration of the simulation. The surface velocity field u is shown in grayscale and offset by a distance from the surface vorticity field. The zoomed-in view shows one of the detached breaking fronts based on Gaussian curvature (see W23 for detail). The vorticity component Ω_z is shown in blue–red color. The blue frame indicates the surface; the purple frame indicates depth $z \approx -3H_s$; the green frame indicates the x–z plane. The same color notation for plane orientation is used in Fig. 5.

moment of $\Lambda(c)$ is theoretically related to wave energy dissipation, which will be discussed in section 5. Finite sample size introduces uncertainty in the statistics, especially for less frequent breakers at large c. We estimate the uncertainty in both $\Lambda(c)$ and $\Lambda(c)c^5$ by further dividing the sample window into four chunks of the same size and compute the maximum and minimum among the four subwindows. The range is indicated by the shading in Fig. 4. More information on the quantification and analysis of the breaking statistics can be found in W23, while here we focus on the underwater dynamics, including current and turbulence generation, as well as energy dissipation.

b. *Characterizing turbulence through vorticity*

The surface layer of the OBL consists of both wave and turbulent motions. It is a real challenge to separate them in field observations, which is another reason why numerical simulations can be valuable. The wave orbital motion is largely irrotational, while the turbulence is characterized by high vorticity. Therefore, we use vorticity as an indicator for turbulence intensity. The vorticity vector $\mathbf{\Omega} = (\Omega_x, \Omega_y, \Omega_z)$ is defined as

$$\mathbf{\Omega} = (\partial_y w - \partial_z v, \partial_z u - \partial_x w, \partial_x v - \partial_y u). \tag{9}$$

We use $\mathbf{\Omega}$ to denote vorticity to distinguish it from the wave angular frequency ω.

As shown by the 3D visualization in Fig. 3 and the 2D slices in Fig. 5, intense patches of vorticity can be found near the surface, with a fast decay at larger depths. At $z \approx -3H_s$ (shown by the purple-framed subplots), only a very weak signature of paired vortices can be seen. Figure 5 also provides a comparison between the least steep (P008) and the moderately steep cases (P02) that we simulated. The least steep case with very infrequent breaking shows much less turbulence generation and shallower penetration compared to the moderately steep case. This demonstrates that the vorticity is indeed generated by breaking-related processes. In the steep cases, intense vorticity generation is concentrated under the breaking crests but seems to be transported further downward by orbital wave motion.

c. *Dissipation rate*

Another quantity of interest is the dissipation rate in the surface layer. In particular, we are interested in the vertical profile of dissipation rate, and how it varies for wave fields of different steepness and thus breaking frequency and intensity. To diagnose the dissipation rate, we compute the strain-rate tensor $\mathbf{S}$, whose components are

$$s_{ij} = \frac{1}{2}\left(\frac{\partial u_i}{\partial x_j} + \frac{\partial u_j}{\partial x_i}\right), \tag{10}$$

where $u_1 = u$, $u_2 = v$, $u_3 = w$ and $x_1 = x$, $x_2 = y$, $x_3 = z$. The dissipation rate (per unit volume) is defined as

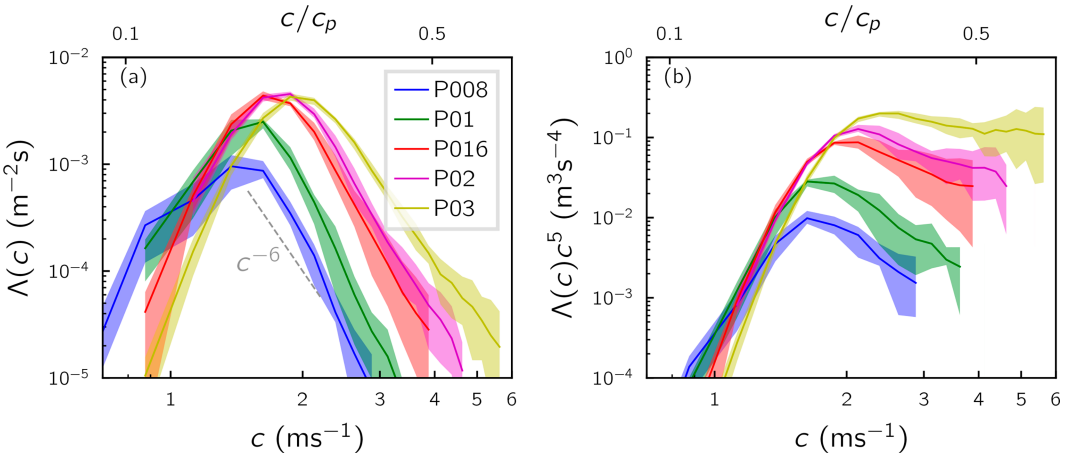

FIG. 4. (a) Breaking distribution $\Lambda(c)$ for increasing wave intensity. (b) Premultiplied breaking distribution $c^5\Lambda(c)$. For both plots, the bottom horizontal axis shows dimensional variables, while the top horizontal axis shows nondimensional variables normalized by peak phase speed c_p.

$$\epsilon \equiv 2\nu s_{ij}s_{ij}, \tag{11}$$

where ν is the viscosity and the Einstein summation convention is used. We can also define a (local) enstrophy $\mathcal{E}$ related to the square of vorticity:

$$\mathcal{E} \equiv \frac{1}{2}\Omega_i\Omega_i. \tag{12}$$

In certain flow regimes, for example, homogeneous high–Reynolds number turbulence, enstrophy is used as a proxy for the dissipation rate in a globally averaged sense (Tennekes and Lumley 1972; Donzis et al. 2008). In other words, $\overline{\mathcal{E}} \approx \overline{s_{ij}s_{ij}}$, where the overline denotes spatial averaging. However, we found that this relation does not apply to the flow simulated here. Figure 6 shows both the enstrophy and the square of the strain-rate tensor. The hotspots of enstrophy are localized and indicate the turbulent region, while the high–strain rate area also includes the near-surface region. In other words, in addition to the turbulence that contributes to the dissipation, there is an area of high strain rate near the free surface due to wave motion, which is an order of magnitude larger than the square of vorticity.

d. Note on choice of vertical coordinate

Due to the difficulties of taking measurements near the moving sea surface, sampling of near-surface turbulence typically needs to be made in a wave-following coordinate system. The dissipation rate measurement and its interpretation might differ based on whether it is made in a wave-following or an absolute vertical coordinate (see e.g., Soloviev and Lukas 2014; Thomson et al. 2016).

We use our simulations as a way to test the effects of vertical sampling choices on mean statistics. To do so, we compute horizontally averaged quantities of interest, denoted with angled brackets $\langle\cdot\rangle$, using both kinds of vertical coordinates (layer or surface following and an absolute or Eulerian vertical coordinate) and plot their vertical profiles in Fig. 7. In the "layer coordinate" (denoted by black lines and markers), we simply average the quantity in each layer l, and use the layer-averaged vertical position $\overline{z_l}$ to draw the 1D profile. This can be considered as approximately wave-following sampling. In the "absolute coordinate" (denoted by blue lines), we interpolate the field onto a regular Cartesian coordinate and then average horizontally. Since the horizontal grid spacing is constant, this interpolation is 1D in z. The horizontal averaging needs further clarification for depths that are not always subsurface (above the gray dashed line around −1.5 m). Label "abs 1" denotes summing the grid points under water and dividing by the area under water (similar to averaging only the crest); label "abs 2" denotes summing the grid points under water and dividing the whole horizontal plane. For a positive-definite quantity such as dissipation rate, an abs 1–averaged value should always be larger than that of abs 2. There is no such ambiguity for the layer coordinate.

Interestingly, the coordinate choice makes a significant difference for analyzing the horizontal velocity profile (Fig. 7a), but not for the vorticity and strain-rate tensor (Figs. 7b,c). This is because when we compute the mean of velocity u in a layer coordinate, we are sampling relatively higher-magnitude positive regions and lower-magnitude negative regions (an effect similar to the origin of Stokes drift). The vertical profile thus becomes a hybrid of Lagrangian and Eulerian mean. This effect is well known in current meters attached to surface-following buoys (Pollard 1973) and is expected to cause a difference equal to half the Stokes drift at the surface, decaying with depth more gradually than the Stokes drift profile, which is qualitatively what we see in Fig. 7a. On the other hand, there is not such correlation between the surface elevation and the turbulence statistics, so the mean of vorticity and strain rate are not affected. We thus use layer averaging in Fig. 9.

To make an order-of-magnitude comparison, we also plot the Stokes drift u_s in Fig. 7a, estimated using Kenyon (1969):

$$u_s(z) = 2g^{1/2}\int k^{3/2}\phi(k)e^{2kz}dk, \tag{13}$$

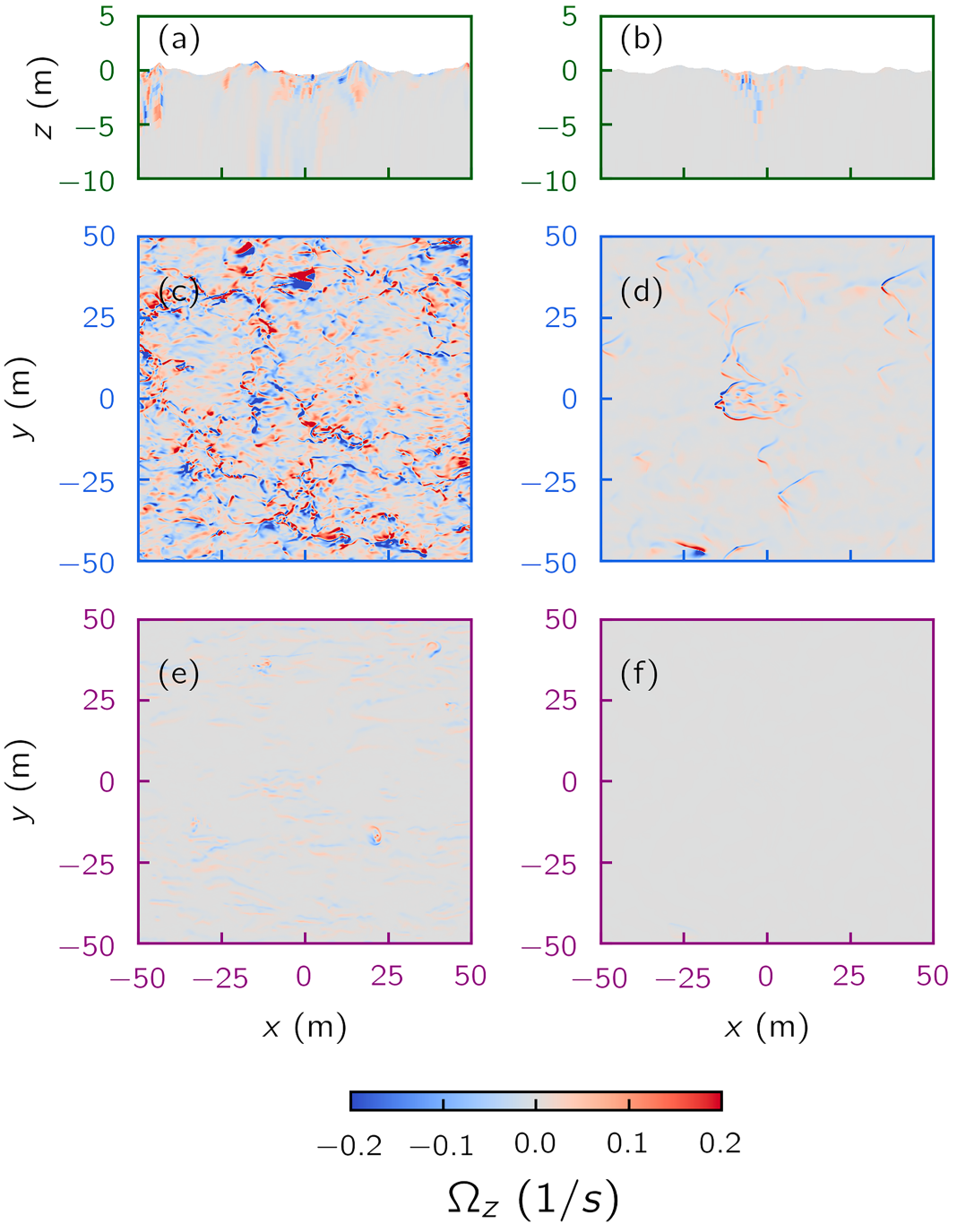

FIG. 5. (a) Instantaneous vertical vorticity field on a zoomed-in slice of the x–z plane at $y = 0$ for the moderately steep case P02 at $t = 120$. (c) Instantaneous vertical vorticity field (zoomed in) in the surface layer for P02 at the same time. (e) Instantaneous vertical vorticity field (zoomed in) in the layer of average depth around $3H_s$ for P02 at the same time. (b),(d),(f) As in (a), (c), and (e), but for the least steep case P008.

where $\phi(k)$ is the unidirectional spectrum. It is worth pointing out that even the strictly Eulerian mean drift current (blue line) is comparable to the Stokes drift, despite being smaller in magnitude and of different vertical structure. This closeness in magnitude might have implications for the estimation of currents on a large scale, which, to our knowledge, has not been widely studied. The current profile in the upper ocean can, of course, be generated through various mechanisms (tide, submesoscale instability, etc.), but here we are isolating the effects of wave breaking.

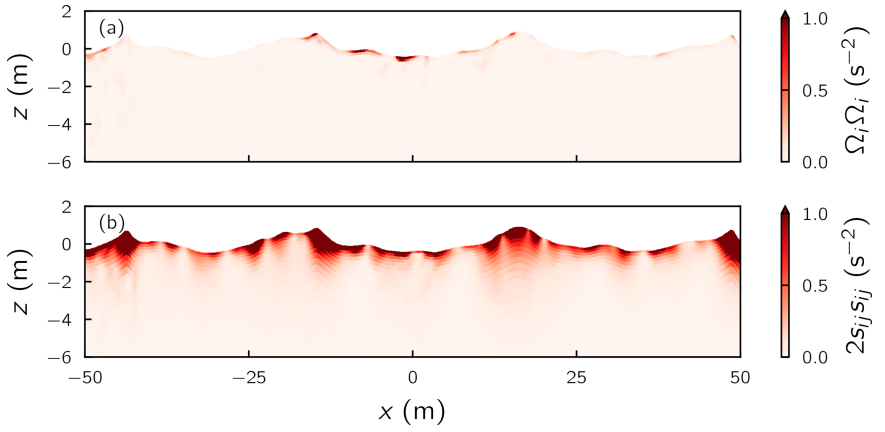

FIG. 6. Instantaneous heatmap of the x–z plane at $y = 0$ and $t = 120$ of (a) enstrophy and (b) square of the strain-rate tensor, from case P02. Dissipation is estimated from the square of the strain-rate tensor.

Finally, for the immediate surface regions that are only partially subsurface, there is a discrepancy between the three different ways of computing the horizontal mean very close to the surface (above −0.5 m). The abs 2 method is the most consistent with flat-surface simulations since it makes sure that the volume-averaged quantities are equal, while the layer method might be closer to the practices in field measurements. As a general caution, near-surface statistics require careful interpretation, as differences in dissipation rates between the layer and absolute averaging methods can approach an order of magnitude.

4. Turbulent boundary layer mean statistics

In the following section, we characterize the underwater breaking-modulated turbulent boundary layer. Again, we focus on the quasi-stationary (developed) stage. First, we comment on the velocity spectrum observed in the simulation. Then, we discuss the scaling of vertical dissipation rate profiles and compare with field observations. We note that even for the developed stage, the time scale considered here is too short for the development of Langmuir turbulence (on the order of 40 wave periods), especially with the lack of a preexisting background current. We thus interpret the results as being representative of conditions dominated by breaking instead of by wave–mean flow interaction or Langmuir turbulence.

a. *Turbulence spectrum*

An advantage of our simulation is that we can directly examine the spatial structure of breaking-generated turbulence, partially represented by the horizontal wavenumber spectra. Observational studies often use turbulence spectra (or, similarly,

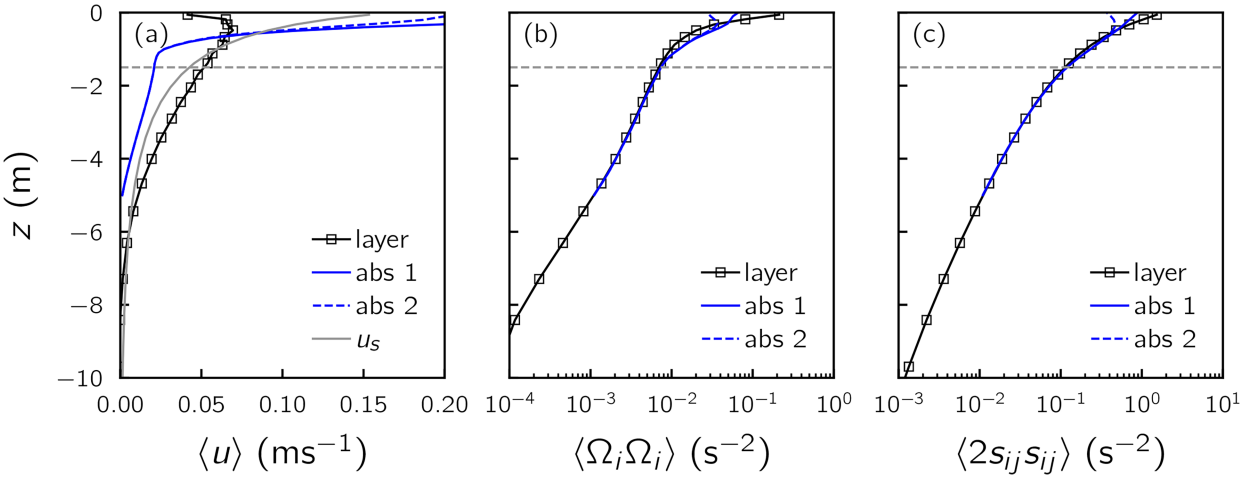

FIG. 7. Vertical profiles of horizontally averaged quantities $\langle\cdot\rangle$ in layer coordinates (squares) vs absolute coordinates (blue lines). For the interpolated absolute coordinate, abs 1 denotes averaging in only the subsurface area, while abs 2 denotes averaging over the whole horizontal area. (a) Velocity component u. The gray solid line shows the Stokes drift computed according to Eq. (13). (b) Enstrophy (times 2). (c) Strain rate squared (times 2). All plots here are for simulations with 30 layers, but cases of $N_L = 15$ and 45 show similar behaviors.

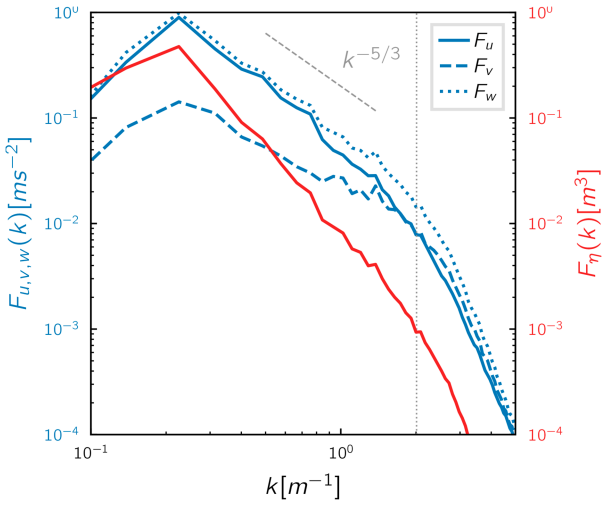

FIG. 8. Spectrum of three velocity components (blue) and surface height spectrum (red). Plotted at the surface layer z = −0.058 m (N_L = 30) during the developed stage. The gray dotted line is the numerical resolution limit calibrated in W23. The gray dashed line indicates the $k^{-5/3}$ power law. Note that the units are not the same for wave energy spectra and velocity spectra.

structure functions) to infer dissipation rate (Gemmrich and Farmer 2004; Thomson 2012; Sutherland and Melville 2015a, etc.), based on theories of the inertial range of isotropic turbulence. However, they are often limited to single-point measurements in time, and, in some cases, the wavenumber spectrum is estimated from the frequency spectrum using Taylor's frozen-field hypothesis. There is also the issue of sampling and measurement uncertainty due to the intermittent nature of turbulent dissipation (Soloviev and Lukas 2003; Sutherland and Melville 2015a) and flow distortion and turbulence generation by the instrument itself (e.g., Zippel et al. 2021).

Since we have the full 3D velocity field, no conversion from frequency to wavenumber spectrum is needed. The 2D spectrum $F(k_x, k_y)$ is calculated in each layer and then azimuthally averaged to get $F(k)$. Only the top layer (at average depth −0.058 m) result is shown in Fig. 8, where blue curves are velocity spectra, and the red curve is the surface wave energy spectrum for comparison.

The velocity spectrum is dominated by wave motion at low wavenumber, again highlighting the challenge of separating wave and turbulence motion (e.g., Gerbi et al. 2009). At higher wavenumber, the velocity spectrum is less steep than the wave spectrum, indicating the presence of small-scale turbulence. Since the turbulence is solely generated by breaking waves, it is clearly anisotropic—fluctuations of the v component (perpendicular to the wave traveling direction) contain lower energy. Spectra of u and w exhibit slopes close to that of an isotropic turbulence spectrum with a $k^{-5/3}$ power law. However, it is in a small range of high wavenumber limited by numerical resolution. Overall, the flow shows strong anisotropy, which brings into question the validity of spectrum-derived estimates of dissipation ϵ that is driven by wave breaking. Therefore, we proceed with using directly computed velocity gradient information (strain-rate tensor) for dissipation rate estimation.

b. *Vertical profile of dissipation and comparison with observations*

Vertical profiles of dissipation rate are often used to compare field measurements with OBL models (Rascle et al. 2013), and they are the focus of our analysis here. The squared strain-rate tensor $\langle s_{ij}s_{ij}\rangle$ provides a direct estimate of dissipation [Eq. (11)] in our simulations. In Fig. 9a, we plot the vertical profiles of layer-averaged squared-strain-rate tensor for different cases in linear–linear scale. With steeper wave fields and more frequent breaking, there is stronger breaking-induced turbulence that extends to greater depths. The rapid decay with depth is highlighted by the linear scale.

In Fig. 9b, the profiles are normalized and shown in log–log scales. The vertical axis z is normalized by significant wave height H_s; the horizontal axis ϵ is normalized by H_s and horizontally averaged, depth-integrated dissipation Ψ, defined as

$$\Psi = \left\langle \int_{-\infty}^{\eta(x,y)} \epsilon dz \right\rangle = \left\langle \int_{-\infty}^{\eta(x,y)} 2\nu s_{ij}s_{ij} dz \right\rangle. \tag{14}$$

This integral has units of cubic meters per cubic second, which is the dissipation rate per unit area per density. Under the choice of H_s and Ψ, simulation cases of varying steepness collapse well, suggesting that H_s and Ψ are suitable scaling parameters and that there may be a universal shape function. We have found that a function,

$$\hat{\epsilon} = 2(|\hat{z}| + 1)^{-3}, \tag{15}$$

describes the data and the shape of the profile well, as shown in the dark gray line in Fig. 9b.

Before discussing the interpretation of this shape function, we compare the normalized profiles to field measurements from AM95, T96, D96, SL03, and SM15. There is a general good agreement between the numerical and observational data in terms of the normalized profiles, despite the fact that the dissipation rate is computed with different methods. In addition, in observational studies, the depth-integrated dissipation rate Ψ is often estimated using a parameterized wave dissipation (further discussed in section 5). The uncertainty in the estimation of Ψ can shift the profiles along the horizontal axis in Fig. 9b, but will not change the general shape of the profile, which is reasonably described by Eq. (15). Also note that most of the published data are sampled around or below $z = H_s$ with the exception of SM15 which measured the surface dissipation (the cloud of data between 0.01 and 0.1 H_s). The vertical resolution of our simulation means that the first layer averages around 0.1 H_s, which prevents a direct comparison with the surface measurements from SM15, but the extrapolated trend seems to agree. We also caution that the surface dissipation rate statistics are sensitive to the averaging method, as shown in the appendix.

Finally, we give an interpretation of the proposed shape function [Eq. (15)] based on the turbulence model outlined in CB94 for the TKE diffusion balancing dissipation regime.

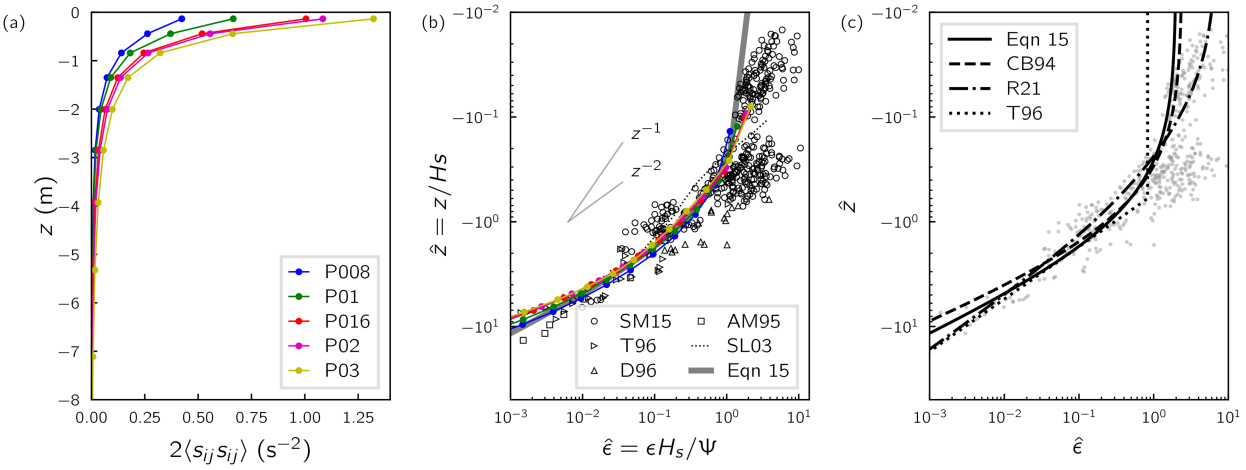

FIG. 9. (a) Layer-averaged squared-strain-rate tensor profiles in linear–linear scale for different cases. (b) Dissipation rate profile in log–log scale normalized by H_s and Ψ. Plotted field observations: Anis and Moum (1995) (AM95), Terray et al. (1996) (T96), Drennan et al. (1996) (D96), Soloviev and Lukas (2003) averaged (SL03), Sutherland and Melville (2015a,b) (SM15). The fitted profile to numerical data [Eq. (15)] is shown in the thick gray line. (c) Proposed nondimensional profile [Eq. (15)] together with existing profiles either from a turbulence model or an empirical fit to observations: Craig and Banner (1994) (CB94), Romero et al. (2021) (R21), and T96. The CB94 is described in the main text. The R21 fit is $0.9508/(4/30 - 8/3\hat{z} + 10/3\hat{z}^2)$. The T96 fit is $\hat{\epsilon} = 0.3\hat{z}^{-2}$ below $z = -0.6\,H_s$ and constant above.

Consider the scenario where the dissipation rate balances the convergence of vertical transport of TKE:

$$\epsilon = \frac{d}{dz}\left(\nu_k \frac{dq^2/2}{dz}\right), \tag{16}$$

where ν_k is the turbulent viscosity (eddy viscosity) and q is the turbulent velocity scale so that TKE $= q^2/2$. On the other hand, dissipation of turbulence is generally assumed to scale with turbulent velocity and length as

$$\epsilon \propto q^3/l = q^3/(Bl), \tag{17}$$

where B is a nondimensional coefficient. In addition, the turbulent viscosity ν_k can be modeled as proportional to the product of turbulent velocity and length scale:

$$\nu_k \propto lq = Slq, \tag{18}$$

where S is another nondimensional coefficient. What remains to close the set of equations to solve for the vertical profile of ϵ is to approximate the length scale l. In the spirit of Prandtl mixing length theory, this length scale is often assumed to be linearly proportional to the distance from the wall:

$$l \propto |z| = \kappa(|z| + z_0), \tag{19}$$

where the slope κ is the von Kármán constant and the intercept z_0 is often termed the roughness length. Combining Eqs. (16)–(19), the resulting equation of ϵ admits a power-law solution (only keeping the decaying part) as

$$\epsilon = C(|z| + z_0)^{-(\lambda+1)}, \tag{20}$$

where the exponent λ is given by a combination of the turbulence model constants as $\lambda = (\kappa^2 BS/3)^{1/2}$, which was estimated by CB94 to be around 2.4. The constant C is given by the surface TKE flux $G = \nu_k[\partial(q^2/2)/\partial z]|_{z=0}$, and the normalized profile for ϵ is

$$\frac{\epsilon z_0}{G} = \lambda\left(\frac{|z|}{z_0} + 1\right)^{-(\lambda+1)}, \tag{21}$$

with the prefactor given by λ as well. Comparing Eq. (21) to the fit to numerical data, Eq. (15), we see remarkably good agreement if using $z_0 \approx H_s$ and $G \approx \Psi$. The fitted exponent $\lambda = 2$ is not far from the one estimated by CB94 using turbulence model constants. The intrinsic relation between the prefactor and the exponent is respected in the data as well.

Based on the above analysis, we conclude that the numerical simulations strongly support two key assumptions in the CB94 model: a dominant balance between dissipation and diffusion of the surface TKE flux [Eq. (16)], and a mixing length that scales linearly with depth but with a nonzero intercept $z_0 \approx H_s$ [Eq. (19)]. This agreement between the simulations and CB94 provides a useful conceptual framework for understanding the effects of wave breaking on surface-layer turbulence. However, it does not preclude alternative (empirical) profile shapes. In Fig. 9c, we compare several early profiles against observational data. Notably, the empirical formulation by R21, which features a second-order polynomial in the denominator, enables a smooth transition between -1 and -2 power laws and fits the near-surface data particularly well. In the immediate vicinity of the surface, our data are compatible with those from SM15 and are slightly larger than the fitted Eq. (15), although the surface-layer statistics seem to be sensitive to averaging methods (see the appendix). Overall, the exact form of the dissipation profile remains insufficiently constrained by observations and may, to some extent, be treated as a modeling choice.

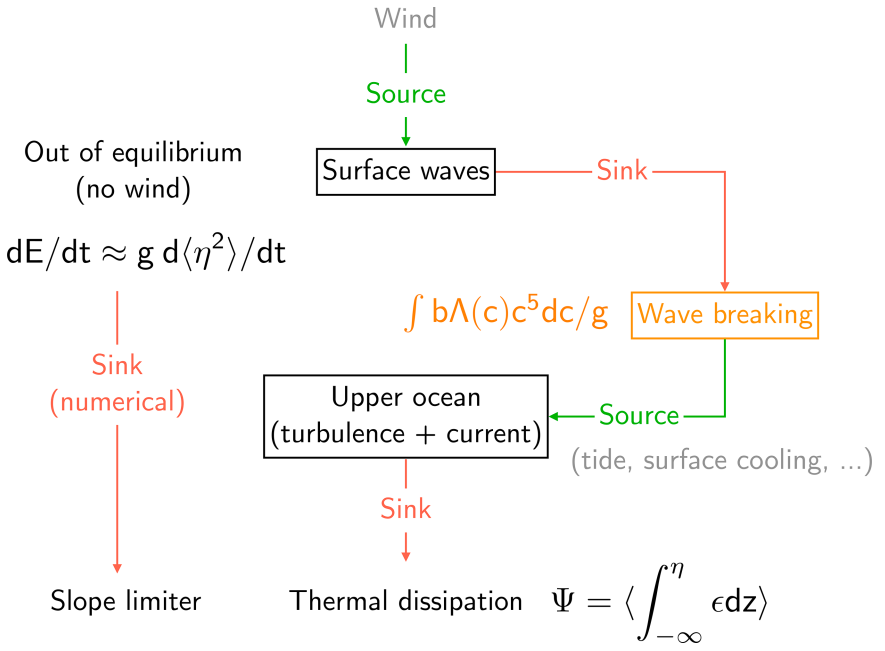

FIG. 10. Flowchart of energy pathways. The dE/dt term, the Ψ term, and the fifth moment term all have the dimension of dissipation rate per unit area per density ($m^3\ s^{-3}$).

5. Energy budget

Finally, we discuss the global energy budget of the system. Figure 10 illustrates the energy pathways between the surface waves and the interior flows (turbulence and current). In reality, the waves gain energy from the wind and dissipate energy through wave breaking. Wave breaking is a source of energy for upper-ocean turbulence (together with other sources), which is eventually dissipated through small-scale thermal dissipation. In the numerical system, there is no wind forcing (in the current setup), and the waves are out of equilibrium. However, the turbulence and current are still in quasi equilibrium with the source of wave breaking balancing the sink of thermal dissipation. In addition, the numerical slope limiter dissipates a certain amount of energy directly.

Based on laboratory-scale experiments and field observations, the dissipation of a broadband wave spectrum can be formulated as (Phillips 1985)

$$S_{ds}(c) = bg^{-1}c^5\Lambda(c). \tag{22}$$

That is, the dissipation at a particular wavenumber (related to c by the dispersion relation) is given by the fifth moment of the breaking distribution times the breaking strength parameter b.

We can diagnose a breaking parameter b for the numerical simulations. Figure 11 shows dE/dt (measured from the energy curves in Fig. 2a), plotted against the fifth moment of $\Lambda(c)$. There is over an order-of-magnitude difference in dissipation rate for cases with different steepness. The corresponding breaking parameter b falls within 0.004–0.015, which is comparable to measured values in laboratory and field. A scale-dependent breaking parameter could also be considered (Romero 2019).

The (sometimes implicit) assumption that the upper-ocean turbulence is in quasi equilibrium leads many field studies to estimate Ψ in Eq. (14) using a spectrally integrated (parameterized) dissipation term S_{ds}. Some works even make a further assumption that the waves are in equilibrium and estimate 14 using an (also parameterized) wind input source term S_{in}. All these implicit assumptions can cause discrepancies for intercomparison between the simulations and observations, and even among observations in different conditions. In the numerical setup, due to the additional dissipative mechanism from the slope limiter, we cannot directly link the global dE/dt to the vertically integrated thermal dissipation. Therefore, we diagnose ϵ directly from the velocity gradient computation in the earlier discussion. Because of the nondimensionalization, the shape of the profile in Fig. 9b should be largely independent from the integrated value of Ψ.

6. Summary and discussion

We applied a novel multilayer numerical solver to broad-banded wave breaking and focused on the structure of underwater breaking-induced turbulence and related dissipation. There is a rich field of vorticity, which is a signature of turbulence generation by breaking waves, since the nonbreaking wave motion is largely irrotational.

An advantage of our numerical simulations is that we are able to sample the full 3D velocity field. We examined the effect of vertical coordinate choice on derived mean statistics, which has implications for field observations. The surface velocity spectra show strong anisotropy and a mix of wave and turbulence signals. Turbulent dissipation is known to be intermittent, and the numerical simulations allow us to compute

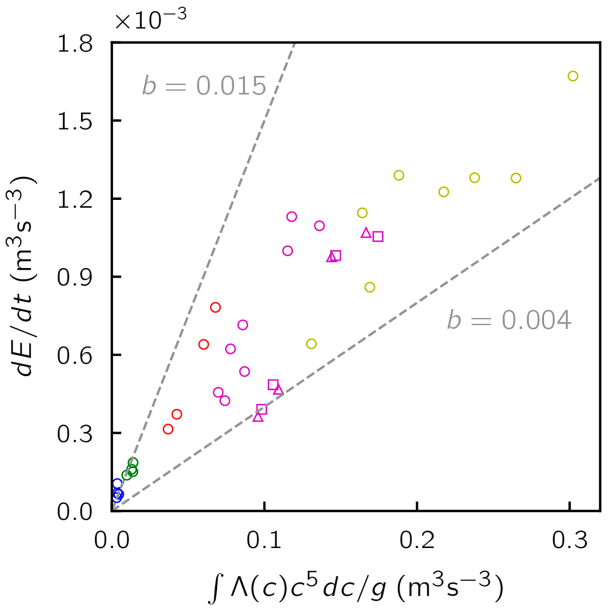

FIG. 11. The energy dissipation (measured from global kinetic and potential energy) vs the fifth moment of $\Lambda(c)$. The colors correspond to different cases. Circles: $N_L = 15$; squares: $N_L = 30$; triangles: $N_L = 45$.

dissipation rate statistics from spatial averaging over a large area, therefore circumventing the potential sampling uncertainty associated with single-point field observations.

We diagnosed the vertical profiles of the dissipation rate directly from the strain-rate tensor and compared them to field observations. The main feature is that strong breaking–induced turbulence is confined to a shallow surface layer and decays very fast below roughly one significant wave height. After normalizing by significant wave height and vertically integrated dissipation, we observed a self-similar profile shape that is well described by $\hat{\epsilon} = 2(1 + \hat{z})^{-3}$. This profile results in a natural transition between the previously debated -1 and -2 power laws over depth. In addition, it compares very well with the analytically derived profile from CB94 and thus provides supporting evidence for the underlying assumptions in their turbulence model: 1) a dominant balance between dissipation and diffusion of surface TKE flux and 2) a mixing length that scales linearly with depth but with a nonzero intercept $z_0 \approx H_s$.

Finally, we relate the global energy dissipation to the breaking front statistics, by which we estimate the approximate range of the breaking coefficient in our numerical setup using linear regression. Although uncertainty still exists, the estimated value of the breaking coefficient is reasonably within the range suggested by existing laboratory and field measurements.

In the context of the ocean surface boundary layer, the layer we describe here is the surface layer, heavily influenced by wind forcing, wave breaking, and wave–turbulence interaction. The current setup was designed to isolate the role of wave breaking in turbulence generation. In reality, there are many mechanisms contributing to the turbulence generation (convection, Langmuir turbulence, near-inertial motion, submesoscale instability, etc.), some of which are able to generate turbulence deeper beyond the surface layer (e.g., Buckingham et al. 2019; Zippel et al. 2022). Our study is idealized and limited because it does not include all these other mechanisms for turbulence generation in the surface layer. However, the idealized setup here is a useful tool to examine the role of wave breaking, allowing us to distinguish the physics of the free-surface boundary layer from the wall layer, precisely because it does not include all these other mechanisms for turbulence generation in the surface layer. Future study will focus on long-term simulations with wind-like surface forcing and a sustained wave field to study the effects of Langmuir turbulence and potentially the interplay between wave breaking and Langmuir turbulence when they coexist.

Acknowledgments. This work is supported by the National Science Foundation under Grant 2318816 to L. D. (Physical Oceanography program) and the NASA Ocean Vector Winds Science Team, Grant 80NSSC23K0983 to L. D. and J. T. F. We thank Peter Sutherland for providing the data and scripts for the turbulence dissipation rate data used in Fig. 9 and originally shown by Sutherland and Melville (2015a).

Data availability statement. The Basilisk solver is open source (http://basilisk.fr/), with the source code in the sandbox (http://basilisk.fr/sandbox/jiarongw/jpo2025/). The specific setup and postprocessing code related to this work can be found at https://github.com/jiarong-wu/multilayer_breaking.

APPENDIX

Sensitivity of Vertical Profiles to Averaging Methods

In the immediate vicinity of the surface, the dissipation rate profile is sensitive to horizontal averaging methods, as shown in Fig. A1. The difference is mainly in the above $0.5H_s$ region and is clearly shown in the log–log scale. In our numerical data, the layer-averaged statistics are closer to those from SM15, while the absolute-coordinate-averaged statistics are closer to a constant line proposed by T96. This sensitivity should be carefully taken into account when comparing observations, numerical simulations, and nonwave-resolving models.

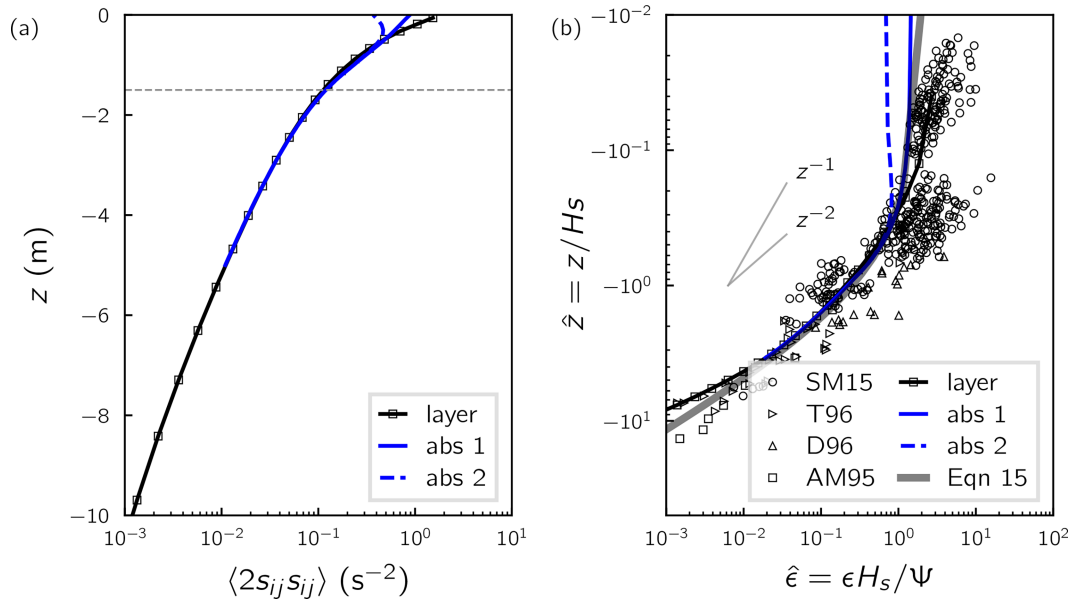

FIG. A1. Sensitivity of the near-surface dissipation rate profile (for the P02 case with $N_L = 30$) to averaging methods: (a) in linear scale (as in Fig. 7) and (b) in log–log scale (similar to Fig. 9 with observational data).

REFERENCES

Anis, A., and J. N. Moum, 1995: Surface wave–turbulence interactions. Scaling $\varepsilon(z)$ near the sea surface. *J. Phys. Oceanogr.*, **25**, 2025–2045, https://doi.org/10.1175/1520-0485(1995)025<2025:SWISNT>2.0.CO;2.

Brocchini, M., and N. Dodd, 2008: Nonlinear shallow water equation modeling for coastal engineering. *J. Waterw. Port Coastal Ocean Eng.*, **134**, 104–120, https://doi.org/10.1061/(ASCE)0733-950X(2008)134:2(104).

Buckingham, C. E., N. S. Lucas, S. E. Belcher, T. P. Rippeth, A. L. M. Grant, J. Le Sommer, A. O. Ajayi, and A. C. Naveira Garabato, 2019: The contribution of surface and submesoscale processes to turbulence in the open ocean surface boundary layer. *J. Adv. Model. Earth Syst.*, **11**, 4066–4094, https://doi.org/10.1029/2019MS001801.

Craig, P. D., and M. L. Banner, 1994: Modeling wave-enhanced turbulence in the ocean surface layer. *J. Phys. Oceanogr.*, **24**, 2546–2559, https://doi.org/10.1175/1520-0485(1994)024<2546:MWETIT>2.0.CO;2.

Donzis, D. A., P. K. Yeung, and K. R. Sreenivasan, 2008: Dissipation and enstrophy in isotropic turbulence: Resolution effects and scaling in direct numerical simulations. *Phys. Fluids*, **20**, 045108, https://doi.org/10.1063/1.2907227.

Drennan, W. M., M. A. Donelan, E. A. Terray, and K. B. Katsaros, 1996: Oceanic turbulence dissipation measurements in SWADE. *J. Phys. Oceanogr.*, **26**, 808–815, https://doi.org/10.1175/1520-0485(1996)026<0808:OTDMIS>2.0.CO;2.

Elfouhaily, T., B. Chapron, K. Katsaros, and D. Vandemark, 1997: A unified directional spectrum for long and short wind-driven waves. *J. Geophys. Res.*, **102**, 15 781–15 796, https://doi.org/10.1029/97JC00467.

Esters, L., Ø. Breivik, S. Landwehr, A. ten Doeschate, G. Sutherland, K. H. Christensen, J.-R. Bidlot, and B. Ward, 2018: Turbulence scaling comparisons in the ocean surface boundary layer. *J. Geophys. Res. Oceans*, **123**, 2172–2191, https://doi.org/10.1002/2017JC013525.

Ferrari, R., and C. Wunsch, 2009: Ocean circulation kinetic energy: Reservoirs, sources, and sinks. *Annu. Rev. Fluid Mech.*, **41**, 253–282, https://doi.org/10.1146/annurev.fluid.40.111406.102139.

Gemmrich, J. R., and D. M. Farmer, 2004: Near-surface turbulence in the presence of breaking waves. *J. Phys. Oceanogr.*, **34**, 1067–1086, https://doi.org/10.1175/1520-0485(2004)034<1067:NTITPO>2.0.CO;2.

Gerbi, G. P., J. H. Trowbridge, E. A. Terray, A. J. Plueddemann, and T. Kukulka, 2009: Observations of turbulence in the ocean surface boundary layer: Energetics and transport. *J. Phys. Oceanogr.*, **39**, 1077–1096, https://doi.org/10.1175/2008JPO4044.1.

Kenyon, K. E., 1969: Stokes drift for random gravity waves. *J. Geophys. Res.*, **74**, 6991–6994, https://doi.org/10.1029/JC074i028p06991.

Kleiss, J. M., and W. K. Melville, 2010: Observations of wave breaking kinematics in fetch-limited seas. *J. Phys. Oceanogr.*, **40**, 2575–2604, https://doi.org/10.1175/2010JPO4383.1.

Kudryavtsev, V., V. Shrira, V. Dulov, and V. Malinovsky, 2008: On the vertical structure of wind-driven sea currents. *J. Phys. Oceanogr.*, **38**, 2121–2144, https://doi.org/10.1175/2008JPO3883.1.

Lenain, L., and W. K. Melville, 2017: Measurements of the directional spectrum across the equilibrium saturation ranges of wind-generated surface waves. *J. Phys. Oceanogr.*, **47**, 2123–2138, https://doi.org/10.1175/JPO-D-17-0017.1.

Miller, U. K., C. J. Zappa, S. F. Zippel, J. T. Farrar, and R. A. Weller, 2023: Scaling of moored surface ocean turbulence measurements in the southeast Pacific Ocean. *J. Geophys. Res. Oceans*, **128**, e2022JC018901, https://doi.org/10.1029/2022JC018901.

Phillips, O. M., 1985: Spectral and statistical properties of the equilibrium range in wind-generated gravity waves. *J. Fluid Mech.*, **156**, 505–531, https://doi.org/10.1017/S0022112085002221.

Pollard, R., 1973: Interpretation of near-surface current meter observations. *Deep-Sea. Res. Oceanogr. Abstr.*, **20**, 261–268, https://doi.org/10.1016/0011-7471(73)90015-6.

Popinet, S., 2020: A vertically-Lagrangian, non-hydrostatic, multilayer model for multiscale free-surface flows. *J. Comput. Phys.*, **418**, 109609, https://doi.org/10.1016/j.jcp.2020.109609.

Rascle, N., B. Chapron, F. Ardhuin, and A. Soloviev, 2013: A note on the direct injection of turbulence by breaking waves. *Ocean Modell.*, **70**, 145–151, https://doi.org/10.1016/j.ocemod.2012.09.001.

Romero, L., 2019: Distribution of surface wave breaking fronts. *Geophys. Res. Lett.*, **46**, 10 463–10 474, https://doi.org/10.1029/2019GL083408.

——, D. Hypolite, and J. C. McWilliams, 2021: Representing wave effects on currents. *Ocean Modell.*, **167**, 101873, https://doi.org/10.1016/j.ocemod.2021.101873.

Schwendeman, M., J. Thomson, and J. R. Gemmrich, 2014: Wave breaking dissipation in a young wind sea. *J. Phys. Oceanogr.*, **44**, 104–127, https://doi.org/10.1175/JPO-D-12-0237.1.

Soloviev, A., and R. Lukas, 2003: Observation of wave-enhanced turbulence in the near-surface layer of the ocean during TOGA COARE. *Deep-Sea Res. I*, **50**, 371–395, https://doi.org/10.1016/S0967-0637(03)00004-9.

——, and ——, 2014: *The Near-Surface Layer of the Ocean: Structure, Dynamics and Applications.* Springer, 552 pp.

Sullivan, P. P., and J. C. McWilliams, 2010: Dynamics of winds and currents coupled to surface waves. *Annu. Rev. Fluid Mech.*, **42**, 19–42, https://doi.org/10.1146/annurev-fluid-121108-145541.

——, ——, and W. K. Melville, 2007: Surface gravity wave effects in the oceanic boundary layer: Large-eddy simulation with vortex force and stochastic breakers. *J. Fluid Mech.*, **593**, 405–452, https://doi.org/10.1017/S002211200700897X.

Sutherland, P., and W. K. Melville, 2013: Field measurements and scaling of ocean surface wave-breaking statistics. *Geophys. Res. Lett.*, **40**, 3074–3079, https://doi.org/10.1002/grl.50584.

——, and ——, 2015a: Field measurements of surface and near-surface turbulence in the presence of breaking waves. *J. Phys. Oceanogr.*, **45**, 943–965, https://doi.org/10.1175/JPO-D-14-0133.1.

——, and ——, 2015b: Measuring turbulent kinetic energy dissipation at a wavy sea surface. *J. Atmos. Oceanic Technol.*, **32**, 1498–1514, https://doi.org/10.1175/JTECH-D-14-00227.1.

Tennekes, H., and J. L. Lumley, 1972: *A First Course in Turbulence.* The MIT Press, 300 pp.

Terray, E. A., M. A. Donelan, Y. C. Agrawal, W. M. Drennan, K. K. Kahma, A. J. Williams, P. A. Hwang, and S. A. Kitaigorodskii, 1996: Estimates of kinetic energy dissipation under breaking waves. *J. Phys. Oceanogr.*, **26**, 792–807, https://doi.org/10.1175/1520-0485(1996)026<0792:EOKEDU>2.0.CO;2.

Thomson, J., 2012: Wave breaking dissipation observed with "SWIFT" drifters. *J. Atmos. Oceanic Technol.*, **29**, 1866–1882, https://doi.org/10.1175/JTECH-D-12-00018.1.

——, M. S. Schwendeman, S. F. Zippel, S. Moghimi, J. Gemmrich, and W. E. Rogers, 2016: Wave-Breaking turbulence in the ocean surface layer. *J. Phys. Oceanogr.*, **46**, 1857–1870, https://doi.org/10.1175/JPO-D-15-0130.1.

Wang, W., and R. X. Huang, 2004: Wind energy input to the surface waves. *J. Phys. Oceanogr.*, **34**, 1276–1280, https://doi.org/10.1175/1520-0485(2004)034<1276:WEITTS>2.0.CO;2.

Wu, J., 2023: Ocean wave dynamics with high fidelity numerical simulations. Ph.D. thesis, Princeton University, 207 pp., https://dataspace.princeton.edu/handle/88435/dsp01tb09j8973.

——, S. Popinet, and L. Deike, 2023: Breaking wave field statistics with a multi-layer model. *J. Fluid Mech.*, **968**, A12, https://doi.org/10.1017/jfm.2023.522.

Zippel, S. F., J. Thomson, and G. Farquharson, 2018: Turbulence from breaking surface waves at a river mouth. *J. Phys. Oceanogr.*, **48**, 435–453, https://doi.org/10.1175/JPO-D-17-0122.1.

——, and Coauthors, 2021: Moored turbulence measurements using pulse-coherent Doppler sonar. *J. Atmos. Oceanic Technol.*, **38**, 1621–1639, https://doi.org/10.1175/JTECH-D-21-0005.1.

——, J. T. Farrar, C. J. Zappa, and A. J. Plueddemann, 2022: Parsing the kinetic energy budget of the ocean surface mixed layer. *Geophys. Res. Lett.*, **49**, e2021GL095920, https://doi.org/10.1029/2021GL095920.